


## Article

# Structural Evaluation of Coal-Tar-Pitch-Based Carbon Materials and Their Na<sup>+</sup> Storage Properties

Ruilin Yin <sup>1</sup>, Kun Wang <sup>1,\*</sup>, Beibei Han <sup>2</sup>, Guiying Xu <sup>1,\*</sup>, Lixiang Li <sup>1</sup>, Baigang An <sup>1</sup> , Dongying Ju <sup>2</sup>, Maorong Chai <sup>2</sup>, Songnan Li <sup>3</sup> and Weimin Zhou <sup>1,\*</sup>

<sup>1</sup> Key Laboratory of Energy Materials and Electrochemistry Research Liaoning Province, University of Science and Technology Liaoning, Anshan 114051, China; lin13050079658@163.com (R.Y.); lxli2005@126.com (L.L.); baigang73@126.com (B.A.)

<sup>2</sup> Advanced Science Research Laboratory, Saitama Institute of Technology, Fusaiji, Fukaya 1690, Japan; hanbeibei@nimte.ac.cn (B.H.); dyju@sit.ac.jp (D.J.); chaimaorong@spic.com.cn (M.C.)

<sup>3</sup> JiXi Weida New Material Technology Co., Ltd., Jixi 158100, China; aabbcc\_2000@126.com

\* Correspondence: wk172860@ustl.edu.cn (K.W.); xuguiying751107@ustl.edu.cn (G.X.); aszhou@ustl.edu.cn (W.Z.)

**Abstract:** Linking to the S element hybrid strategies, S-doped carbon materials having different macrostructures and defect concentrations are prepared by using sulfur and coal-tar-pitch as raw materials in a carbonization temperature range of 700–1000 °C. The evaluations of macrostructure and surface characteristics are performed through XRD, TEM, Raman and XPS measurements. Through the linear fitting among the Na<sup>+</sup> storage capacity with I<sub>D</sub>/I<sub>G</sub> and d<sub>002</sub> values, the correlations of Na<sup>+</sup> storage capacity with macrostructures and defects are respectively investigated in detail. It is observed that S-doped carbon materials exhibit storage capacity at 120 mAh/g after the charge-discharge is being carried out 2000 cycles at 2.0 A/g. Studies have shown that adsorptions of introduced defects on graphene-like carbon sheets mainly play the role to enhance the storage capacity, and the expanded carbonaceous lamellar spaces of highly disordered and pseudo-graphitic macrostructures provide the channels for fast transfer of Na<sup>+</sup>. Our studies are able to provide references for designs and fabrications of coal tar pitch based soft carbon materials as sodium-ion batteries (SIBs) anodes when using heteroatoms doping methods.

**Keywords:** coal-tar-pitch; sodium-ion batteries; Na<sup>+</sup> storage capacity; soft carbon materials; structure-activity relationship



**Citation:** Yin, R.; Wang, K.; Han, B.; Xu, G.; Li, L.; An, B.; Ju, D.; Chai, M.; Li, S.; Zhou, W. Structural Evaluation of Coal-Tar-Pitch-Based Carbon Materials and Their Na<sup>+</sup> Storage Properties. *Coatings* **2021**, *11*, 948. <https://doi.org/10.3390/coatings11080948>

Academic Editor: Je Moon Yun

Received: 17 June 2021

Accepted: 2 August 2021

Published: 8 August 2021

**Publisher's Note:** MDPI stays neutral with regard to jurisdictional claims in published maps and institutional affiliations.



**Copyright:** © 2021 by the authors. Licensee MDPI, Basel, Switzerland. This article is an open access article distributed under the terms and conditions of the Creative Commons Attribution (CC BY) license (<https://creativecommons.org/licenses/by/4.0/>).

## 1. Introduction

On the basis of the fact that Na element shows tremendous reserves, sodium-ion batteries (SIBs) are becoming the preferred storage system used to construct energy storage systems (ESSs) more than ever before [1–3]. In contrast to the developments of studies about positive electrodes, the studies about anode materials are relatively slow, which dominates commercialization processes of SIBs.

It is already found that a lot of materials such as titanate, alloys, metal oxides, sulfides and carbon materials are suitable as anode materials to assemble SIBs. Thereinto, carbon materials have attracted more attention than other options because of they have desirable characteristics such as low cost, environmental friendliness, facile fabrication and so on [4–8].

In general, the carbon materials are classified into hard carbon and soft carbon materials, respectively. Among them, hard carbon materials are generally constructed from carbonaceous sheets having unordered structures. As anode materials hard carbon materials display excellent characteristics in that the most of their high storage capacity is shown at low potential plateaus, leading to the fact that the assembled SIBs manifest a high energy density. The sodium storage mechanism of hard carbon was systematically summarized by Guo et al. [9,10]. The many storage mechanism models such as “insertion–absorption”,

adsorption–insertion”, “adsorption–nanopore filling”, “adsorption–insertion and nanopore filling” are introduced in detail. The proposal of storage mechanisms exhibits the guiding significance for development of hard carbons as electrode materials.

Nevertheless, this high storage capacity disappears almost completely at big current density, resulting in the observation that their rate performances are unsatisfactory in actual applications. Additionally, when the cells run at high-rate performance and low temperature, sodium dendrites usually form in the potential plateaus area, causing a hidden danger the unavoidably appears. These problems restrict the actual applications of hard carbon materials in the fabrication of SIBs [11].

In comparison with hard carbons, the carbon layers in soft carbon materials manifest ordered structures, and their capacity–voltage curves show a tilting behavior. Meanwhile, the conductivity of soft carbons is better than that of hard carbons. The aforementioned excellent properties lead to soft carbons having tremendous rate performances. Therefore, soft carbons are considered to be suitable carbon materials to fabricate SIB anode materials. Wang pointed out that pitches are fabulous materials to fabricate SIB anodes as pitches made up of polycyclic aromatic hydrocarbons (PAHs) easily become carbons having abundant graphite-like crystallites, when carbonization processes are being performed [12]. Nevertheless, the  $\text{Na}^+$  ions insert with difficulty into microcrystalline graphites, restricting in an increase of storage capacity. Thus, how to regulate the structures of microcrystalline graphites is becoming the hot research topic to enhance the storage capacity of soft carbons. Some methods are developed and utilized to fabricate SIB electrodes. For instance, the template methods are the one of most effective methods to construct suitable structures to store  $\text{Na}^+$  ions [13–15]. Besides, heteroatom doping is another effective way to construct structures to store  $\text{Na}^+$ , which is a topic also studied by a lot of research groups.

In our studies, to effectively design and develop the carbon materials to store  $\text{Na}^+$ , we have attempted to explore the essential factors that influence the construction of carbon material structures for storing  $\text{Na}^+$ . Thus, we choose the S-doping case to investigate the correlations between the structures and  $\text{Na}^+$  storage capacity in detail [16]. This is different from the approach reported by He et al. [16], in that we pay more attention to the research about structure–activity relationships that are produced by doping the S element into coal tar pitch-based carbons. In other words, through detailed analyses of the relationship between the  $\text{Na}^+$  storage capacity and structures, we attempt to deeply understand the storage mechanism of S-doped soft carbon materials. As a result, it is observed that cooperative effects which are the expansion of  $\text{Na}^+$  transfer channels and introduced defects play the main role to enhance the  $\text{Na}^+$  storage capacity. These observations from our studies probably provide a useful reference to design and develop carbon anode materials for the fabrication of SIBs.

## 2. Materials and Methods

### 2.1. Characteristics

The measurements of X-ray diffraction (XRD) used an X’pert Powder instrument from PANalytical (Almelo, Overijssel, The Netherlands). The X-ray photoelectron spectroscopy (XPS) measurements were carried out on a K-Alpha instrument from Thermo Fisher Scientific, (Waltham, MA, USA). Nitrogen adsorption and desorption isotherms was measured by a Quadrasorb autosorb-iQ surface analyzer which was purchased from Quantachrome Instruments (Boynton Beach, FL, USA). Specific surface areas were determined in detail, according to the Brunauer–Emmett–Teller (BET) method. The pore size distribution was assessed by a DFT model for slit pores. Morphologies were evaluated by scanning electron microscopy (SEM) using an instrument produced by Carl Zeiss AG, (Oberkochen, Badensko-wuertembersko, Germany). TEM measurements were carried out on a HF-3300 system (Hitachi Co. Ltd., Tokyo, Japan). The FT-IR measurements were performed on an ALPHA II spectrophotometer (Bruker Co. Ltd., Karlsruhe, Badensko-wuertembersko, Germany). The elemental analyses were carried out by using a UNICUBE (Elementar Analysensysteme GmbH, Langenselbold, Hesse-Darmstadt, Germany). Electrochemical

measurements were performed by a CHI660E electrochemical system (ChenHua, Shanghai, China). Thermogravimetric analysis (TGA) measurements were carried out by using a TG209F3 (NETZSCH, Selb, Bayern, Germany).

## 2.2. Preparations of Coal-Tar-Pitch-Based Carbon Materials

The coal tar pitches were ground to under 100  $\mu\text{m}$ , and then they were placed in a tube furnace with a heating rate of 3  $^{\circ}\text{C}/\text{min}$  and carbonized at 700, 800, 900 and 1000  $^{\circ}\text{C}$ , respectively, for 2 h in a  $\text{N}_2$  atmosphere. According to the different carbonization temperatures, the obtained materials were identified as 700-PC, 800-PC, 900-PC and 1000-PC, respectively.

## 2.3. Preparation of S-Modified Coal-Tar-Pitches

The coal tar pitches were mixed with elemental S in a weight ratio of 1:1, and then they were ground under 100  $\mu\text{m}$ . The obtained mixtures were placed in reactors and stirred for 2 h in a  $\text{N}_2$  atmosphere at 200  $^{\circ}\text{C}$ . After cooling the reactor to room temperature, the S-modified coal-tar-pitch was obtained.

## 2.4. Preparations of S-Modified Coal-Tar-Pitch-Based Carbon Materials

The prepared S-modified coal-tar-pitches were placed in the oven and carbonized for 2 h in a flow of  $\text{N}_2$  (100 mL/min) at temperatures of 700, 800, 900 and 1000  $^{\circ}\text{C}$ , respectively. According to the carbonization temperatures, the finally obtained S-doped materials were named as 700-SPC, 800-SPC, 900-SPC and 1000-SPC, respectively.

## 2.5. Electrochemical Measurements

The electrochemical cells were assembled by using the prepared composite materials. Firstly, active materials (0.08 g) mixed with acetylene black (0.01 g) and polyvinylidene fluoride (PVDF) binder (0.01 g) in a weight ratio of 80:10:10 in N-methyl-2-pyrrolidone (NMP) solution. The prepared slurry was placed on a Cu foil and dried in a vacuum drying oven at 80  $^{\circ}\text{C}$  for 1 h to remove the solvent. The Cu foils with the active materials (1.2  $\text{mg}/\text{cm}^2$ ) were continuously dried at 120  $^{\circ}\text{C}$  for 12 h in the same vacuum drying oven and cut into round shaped strips of  $\phi$  11 mm in size. The cells were assembled with sodium of  $\phi$  11 mm size, as active materials for the negative electrode and electrolyte of a mixed solution of 1M  $\text{NaClO}_4$  with EC and DMC (1:1). Cyclic voltammetry (CV) and electrochemical impedance spectroscopy (EIS) measurements were carried out using the CHI 660E, ChenHua, Shanghai, China). The CV curves were recorded in the voltage region of 0.01–3.00 V.

## 3. Results

Before carbonization, the structures of S-modifying pitches were firstly investigated by X-ray photoelectron spectroscopy (XPS), X-ray diffraction (XRD, Almelo, Overijssel, The Netherlands) and thermogravimetric analysis (TGA, NETZSCH, Selb, Bayern, Germany) measurements. As per Figure 1a, it is clear that the pristine pitch materials are made up of the elements C and O. By contrast, the element S was distinctly observed in the S-modified pitches. After the peak of S2p had been fitted, the existence of  $-\text{C}-\text{S}_x-\text{C}-$  bonding type was observed clearly in S-modified pitches (Figure 1b) [17]. Meanwhile, as shown in Figure 1c, comparing the characteristic curves of sulfur, the fact that free sulfur did not exist in S-modified pitches was observed, indicating that elemental S element of a bound type mainly exists in the S-modified pitches.

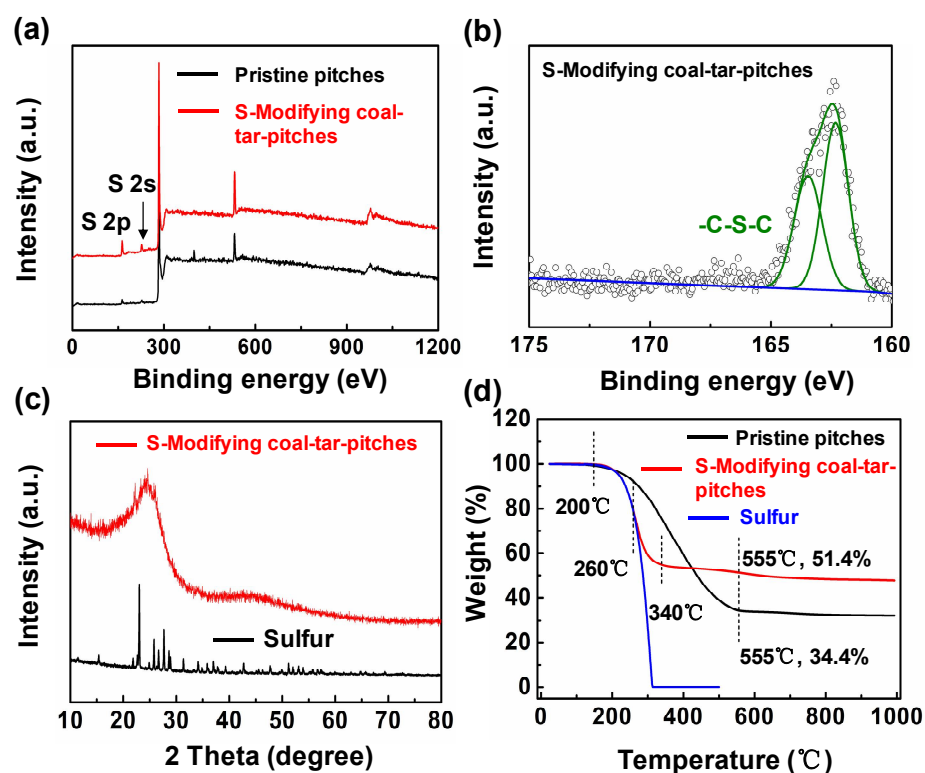


**Figure 1.** XPS results of pristine pitch and S-modifying coal-tar-pitches (a), Fitting result of the XPS data of S-modifying coal-tar-pitches (b). XRD results of S-modified coal-tar-pitch and sulfur (c). TGA results of pristine pitch, S-modified coal-tar-pitch and sulfur (d).

The evidence that S element exists in the S-modified pitches was further supported by the TGA measurements (Figure 1d). In the treatment case of pristine pitch materials, the quick weight loss appearing at 200–555 °C is attributed to the pyrolysis process occurring during carbonization [11]. After the temperature rose to the 555 °C, the rate of weight loss became slow because of the content of low molecular weight compounds in pristine pitches was very small. Comparatively, a quick weight loss at 200–340 °C was observed in the S-modified pitches. The relatively low final temperature of 340 °C can probably be ascribed to the fact that the S is present in bound form in S-modified pitches. The phenomenon that the two curves of sulfur and S-modified pitches overlapped approximately in the temperature range (25–260 °C) is also suggestive of the fact elemental S exists in the S-modified pitches. In addition, when the temperature was increased to 555 °C, the weight retention of S-modifying pitches was 51.4% which was higher than that of pristine pitch materials (34.4%) which also revealed that elemental S was successfully doped in the S-modified pitches.

The obtained S-modified pitches next underwent a carbonization process to fabricate S-doped pitch-based carbon materials (SPC). To better understand the structural conversions of SPC, investigations on the pitch-based carbon materials (PC) were also conducted in detail. Because of the defect concentrations in structures generally influence the Na<sup>+</sup> storage capacity, the chemical states were explored by XPS measurements in detail [11,18,19]. As shown in Figure S1, the PC materials are mainly constructed by the element C and O. Furthermore, the changes of O contents in PC materials were also analyzed through XPS measurements (Figure S1a). The O contents of 700-PC, 800-PC, 900-PC and 1000-PC were calculated at 11%, 9.7%, 8.3% and 6.9%, exhibiting an obvious decreasing tendency (Figure S1b). Meanwhile, the O 1s peak can be fitted to three 531.6, 532.6 and 533.8 eV peaks, corresponding to C=O, C–O and –COOH groups, respectively [17,20]. In particular it is observed that the contents of –COOH remarkably diminished, compared with the C=O and C–O groups (Figure S1c–f, Table S1).



SPC materials are mainly made of the elements C, O, S, which can be observed in Figure 2. It is notable that cross-linked forms such as C-S<sub>x</sub>-C, C-SO<sub>x</sub>-C and C=S also exist in our prepared carbon materials (Figure 2c–f) [16,20,21]. It is observed that the C=S peaks do not appear in the 700-SPC (Figure 2c), but their characteristic peaks appeared with increasing carbonization temperature, and their peak intensities show an obvious increasing tendency (Figure 2d–f). In contrast, the contents of -C-S-C-, -S-O groups manifest a diminishing tendency.

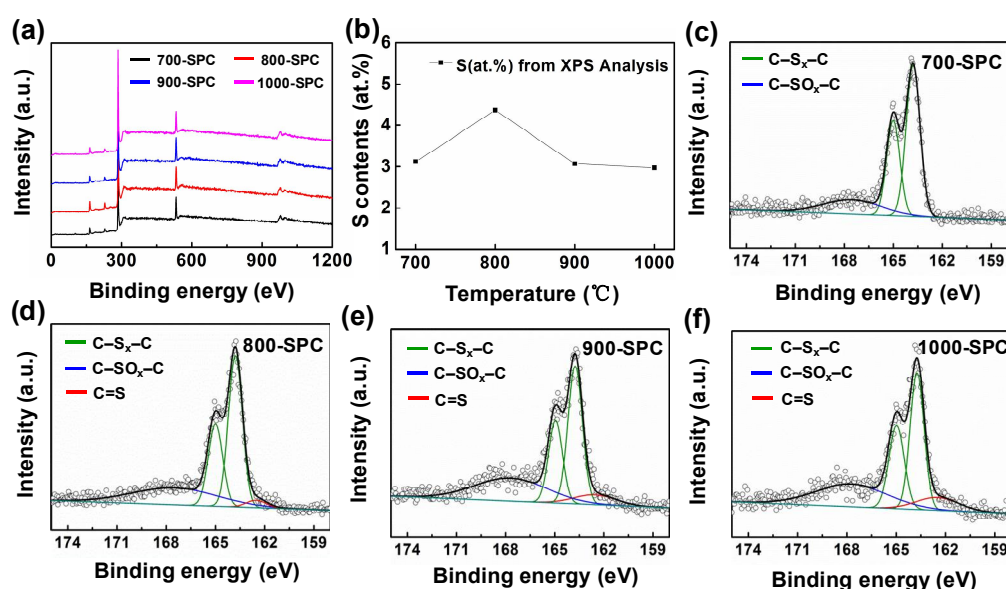


**Figure 2.** XPS results of SPC materials. (a). (b) are the S contents calculated according to the XPS results. (c–f) are the fitting results of SPC materials.

The concentration of O and S elements in SPC materials are calculated and illustrated as shown in Table S2. As a result, it is observed that SPC-800 possesses a higher contents of O and S elements than other materials, indicating the defect concentrations of 800-SPC are more than in the other materials (Table S2). Figure 2b exhibits that 800-SPC possesses a higher S content than other SPC materials. In addition, the elemental analysis results also indicate that 800-SPC possesses a higher content of S element than other materials (Table S3).

On the other hand, the FT-IR results can describe in detail the conversions of groups containing S element (Figure S2). Compared with the peak intensities (around 1580 cm<sup>-1</sup>) of aromatic groups, the peak intensities of S-O (1067 cm<sup>-1</sup>) and C-S (667 cm<sup>-1</sup>) groups in SPC materials are remarkably stronger than those in PC materials, indicating that S-O and -C-S-C- groups increased in SPC materials (Figure S2).

The structural characteristics of PC and SPC materials are investigated by XRD measurements in detail (Figure 3). The fact that the characteristic peaks sulfur are not observed in SPC materials leads us to consider that the elemental S which was added into carbon materials exists in chemically bonded form, which indicates that doping the element S in carbon materials is not simply a mixing process (Figure S3b). Generally, the two characteristic peaks around 24° and 43° correspond to disordered carbon and microcrystalline carbon, respectively. In the case of PC materials, increasing the carbonization temperature, the peaks around 24° in PC materials are shifted to higher degrees, which indicates that the structures of PC materials became ordered (Figure S3a). However, the same phenomenon was not observed in the SPC materials, which also indicated that introducing S in pitches caused their structures to become disordered, although the carbonization temperature was increased (Figure S3b). Furthermore, as shown in Figure 3, compared with PC materials, the peaks around 24° of SPC materials shifted to smaller degrees, indicating that the S doping method caused the structures of SPC materials to become disordered.

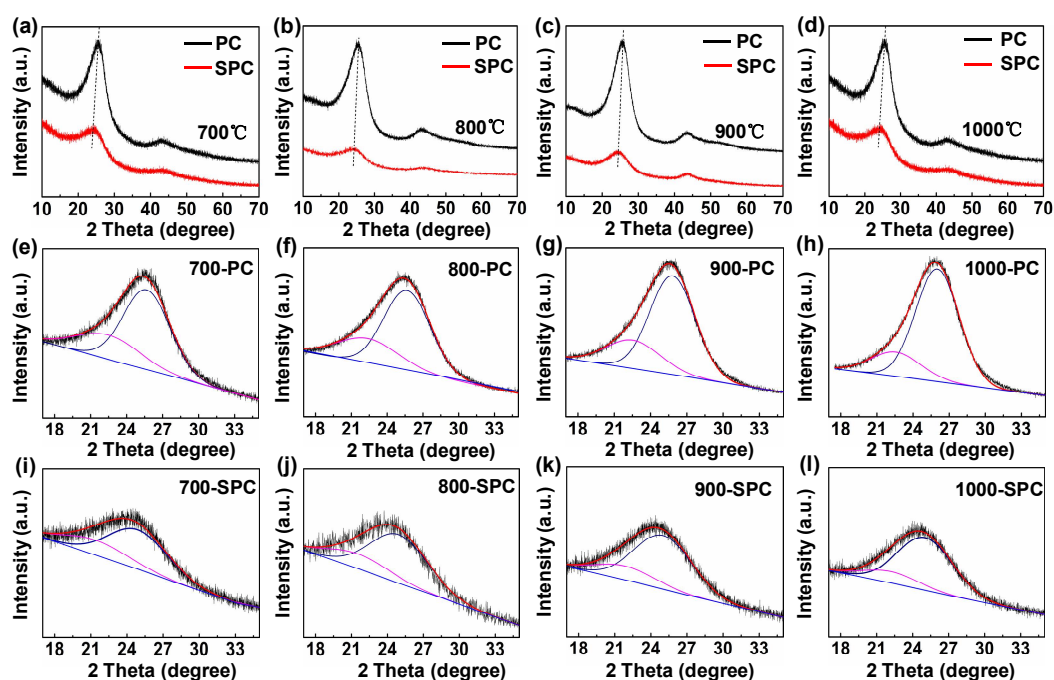


Figure 3. XRD results (a–d) and their fitting results of PC and SPC materials (e–l).

In addition, R values (obtained by calculation according to the XRD measurement results) are generally used to describe the degree of disorder [22,23]. Namely, low R values reflect that carbon materials possess a disordered structure. Like the report of Liu et al., and based on the XRD results (Figure 3e–i), the R values were calculated in detail [22]. As shown in Figure 4, the R values of PC and SPC materials show similar tendencies whereby the R values decrease with decreasing carbonization temperature. In addition, compared with the PC materials, it is seen that the SPC materials exhibit more disordered structures (Table S4). In particular, the 800-SPC material showed the smallest R value of all materials, which is ascribed to the fact that 800-SPC possesses more S contents than other SPC materials (Figure 4, Table S4).

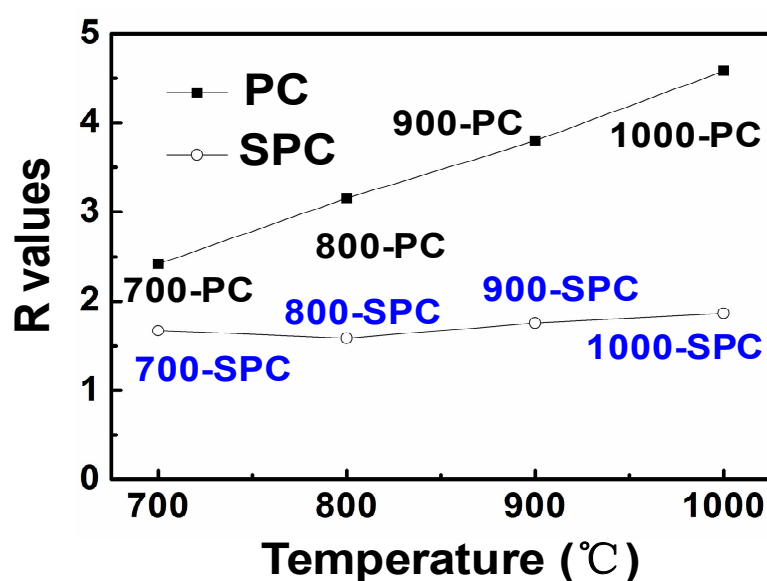


Figure 4. R values of PC and SPC materials.

To investigate the structures of PC and SPC materials further, Gaussian fitting is used to analyze their structures in detail. In general, the microstructures are classified into three types [24,25]: (1) is the highly disordered type. It leads to the diffusion barrier approaching zero, when the  $d_{002,a}$  is bigger than 0.4 nm [25]. (2)  $d_{002,a}$  is a pseudo-graphitic type, generally shown at 0.35–0.4 nm, which is satisfy to necessity of  $\text{Na}^+$  storage [26]. (3)  $d_{002,a}$  of graphite-like microstructures is generally smaller than the 0.35 nm, leading to difficulty for  $\text{Na}^+$  to insert into carbon sheets. Thus, as shown in Table 1, the fact that PC carbon materials are mainly constructed by pseudo-graphitic and graphite-like microcrystalline forms was distinctly observed. Meanwhile, in PC materials, it is noticeable that the pseudo-graphitic ratio diminished from 29.1% to 19.8%, however, the contents of graphite-like carbons increased from 70.9% to the 80.2%. Meanwhile, the fact that  $L_{c,a}$  expanded from 1.71 to 1.95 nm was also determined obviously (Table 1). These results reveal that the structures become ordered and the stacking height among the (002) crystal phase grows slowly.

Table 1. Physical Parameters of Different Samples.

| Samples  | Highly Disordered |                   |             | Pseudo-Grphitic |                   |             | Graphite-Like |                   |             | $d_{002,a}$<br>(nm) | $L_{c,a}$<br>(nm) |
|----------|-------------------|-------------------|-------------|-----------------|-------------------|-------------|---------------|-------------------|-------------|---------------------|-------------------|
|          | $2\theta$ [°]     | $d_{002}$<br>[nm] | Area<br>[%] | $2\theta$ [°]   | $d_{002}$<br>[nm] | Area<br>[%] | $2\theta$ [°] | $d_{002}$<br>[nm] | Area<br>[%] |                     |                   |
| 1000-PC  | -                 | -                 | -           | 22.59           | 0.394             | 19.80       | 26.01         | 0.343             | 80.20       | 0.353               | 1.95              |
| 900-PC   | -                 | -                 | -           | 22.57           | 0.394             | 25.84       | 25.82         | 0.345             | 74.16       | 0.358               | 1.85              |
| 800-PC   | -                 | -                 | -           | 22.50           | 0.395             | 28.50       | 25.77         | 0.346             | 71.50       | 0.360               | 1.80              |
| 700-PC   | -                 | -                 | -           | 22.42           | 0.396             | 29.14       | 25.67         | 0.347             | 70.86       | 0.361               | 1.71              |
| 1000-SPC | 22.11             | 0.402             | 17.75       | 25.01           | 0.356             | 82.25       | -             | -                 | -           | 0.364               | 1.58              |
| 900-SPC  | 21.84             | 0.407             | 20.82       | 24.99           | 0.356             | 79.18       | -             | -                 | -           | 0.367               | 1.50              |
| 800-SPC  | 21.43             | 0.415             | 24.31       | 24.95           | 0.357             | 75.69       | -             | -                 | -           | 0.371               | 1.44              |
| 700-SPC  | 21.43             | 0.415             | 22.19       | 24.95           | 0.357             | 77.81       | -             | -                 | -           | 0.369               | 1.47              |

$d_{002,a}$ : is the value of the average interplanar spacing;  $L_{c,a}$  are the values of average stacking heights of coal chars.

Likewise, a similar tendency was also observed in the SPC materials. Interestingly, the  $d_{002,a}$  of 1000-SPC was smaller than that of the other SPC materials, however, this value was significantly higher than that of all of PC materials, which was strongly supportive of the notion that S causes a significant ordering of microcrystallines during carbonization processes.

The aforementioned evaluations were also verified by the TEM measurements. As shown in Figure S4, the phenomenon that the selected area electron diffraction (SAED) patterns display tendencies which range from blurry to clear is also suggestive of the fact that the structures of microcrystallites become ordered with increasing carbonization temperature [27,28]. On the other hand, with the introduction of elemental S the SAED patterns became indistinct (Figure S5). Especially, compared with the local zoom, we can observe that the 800-PC materials have obvious parallel lamellar structures, and the 800-SPC materials show obvious turbine-like structures, which can probably be ascribed to the doped S element influencing the growth along the parallel direction of the carbon sheets (Figure 5).

Nevertheless, no obvious differences in SEM morphologies of PC and SPC materials were clearly observed (Figure S4). Namely, the PC and SPC materials both displayed sheet-like morphologies. Additionally, the SEM-EDS measurement results provide clear evidence that the elements O and S are homogenously dispersed on the surface of SPC-800, which enables to facilitate the SPC materials to enhance the  $\text{Na}^+$  storage capacity (Figure S4i–j).

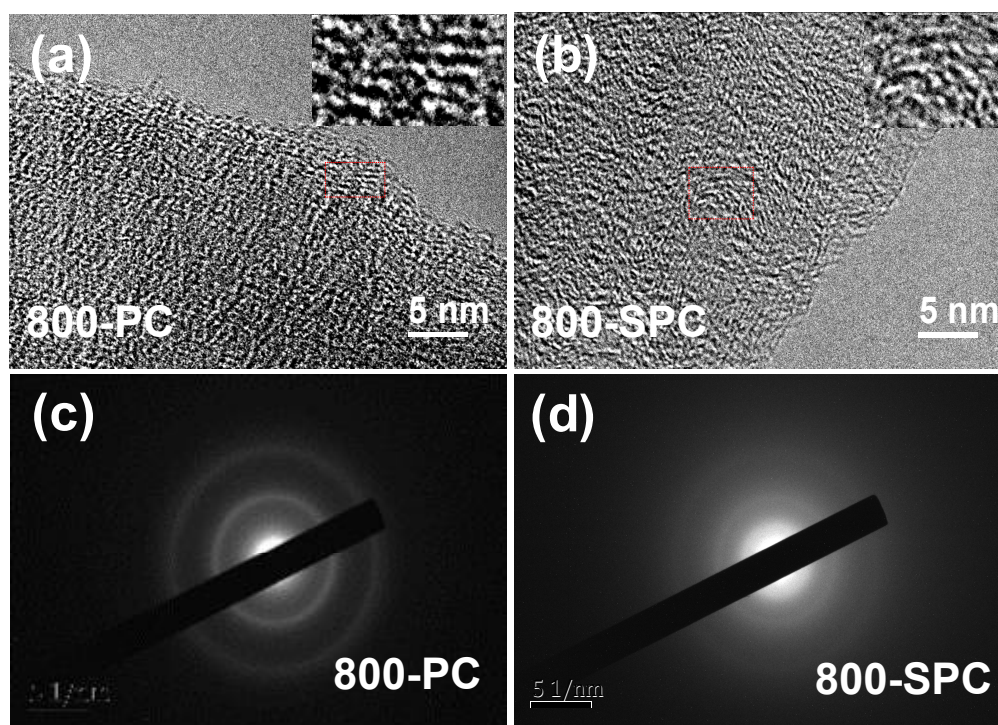


**Figure 5.** TEM images of PC (a) and SPC (b) materials. Selected area electron diffraction (SAED) patterns of PC (c) and SPC (d) materials.

The porosities of PC and SPC materials were evaluated by the BET method. It is found that the SPC materials showed a bigger specific surface area and more complex porous structures than PC materials (Figure S7 and Table S5). This naturally leads us to consider that the aforementioned phenomena can be attributed to the introduction of elemental S into coal tar pitch-based carbons.

To prop up the abovementioned analyses, Raman measurements were performed in detail (Figure S8). It is acknowledged that  $I_D/I_G$  can reflect the degree of disorder of carbon materials [29,30]. As shown in Table S6, the 800-SPC possesses a more disordered structure than the other forms. Meanwhile, the 800-SPC exhibited a  $L_a$  value calculated by Raman results at 6.72 nm, which is smaller than that of the other materials, again confirming resulting in has a more disordered structure than other materials (Table S6).

The general electrochemical evaluations were used to understand the correlations between the structures and  $\text{Na}^+$  storage capacity. As shown in Figure S9a,c, the sodium storage abilities of PC and SPC materials were respectively shown at 104 mAh/g (1000-PC), 120 mAh/g (900-PC), 131 mAh/g (800-PC), 135 mAh/g (700-PC), 151 mAh/g (1000-SPC), 216 mAh/g (900-SPC), 333 mAh/g (800-SPC), 284 mAh/g (700-SPC) at a current density of 0.1 A/g on the first cycle. In addition, the materials of 1000-PC, 900-PC, 800-PC, 700-PC, 1000-SPC, 900-SPC, 800-SPC and 700-SPC exhibited a storage capacity of 57 mAh/g, 68 mAh/g, 88 mAh/g, 91 mAh/g, 82 mAh/g, 115 mAh/g, 210 mAh/g and 169 mAh/g, respectively, after performing 100 charge-discharge cycles at 0.5 A/g (Figure S9a,c). It is worth paying attention to the fact that the SPC materials showed more excellent storage capacity than PC materials (Figure S9b,d). Considering fact that PC materials possessed more ordered structures than the SPC materials, we naturally think that the increased degree of order is not beneficial to storing the  $\text{Na}^+$ .

In particular, 800-SPC exhibits a higher reversible capacity at 333 mAh/g and a Coulombic efficiency of 61.2% in the first cycle. The relatively low Coulombic efficiency is generally attributed to the formation of a solid electrolyte interphase (SEI) [31–33]. As shown in Figure S9d, the 800-SPC displayed much better rate performances than other SPC materials. Namely, 800-SPC manifested a more excellent  $\text{Na}^+$  storage capacity than other



SPC materials at different current densities which were changed from 0.1 A/g to 2.0 A/g, and then recovered to 0.1 A/g (Figure S9d).

Based on the fact that 800-SPC possesses better cycling performance and rate performance than other PC and SPC materials (Figure S9), an evaluation of the long cycling performance of 800-SPC at a big current density (2 A/g) was performed. After charge-discharge had been performed for 2000 cycles, 800-SPC still exhibited a storage capacity at 120 mAh/g when the current densities were set at 2.0 A/g (Figure 6), so in comparison with the other reported materials, 800-SPC also exhibited excellent storage capacity (Table S7).

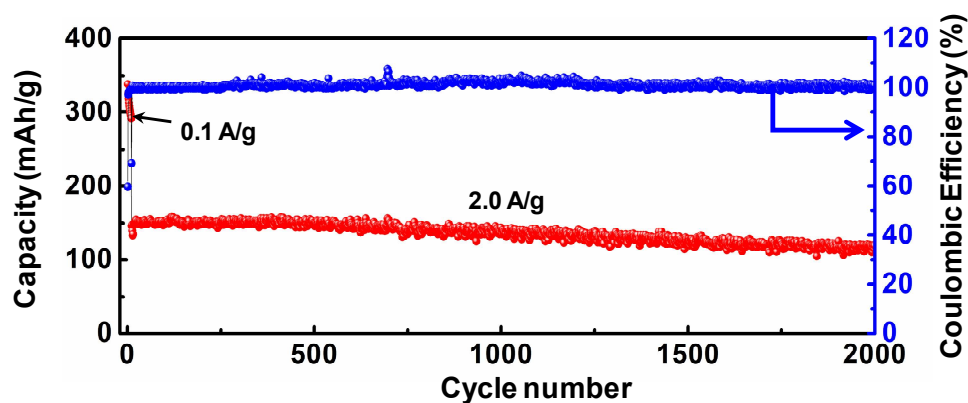


Figure 6. Cycling performance of 800-SPC material at current density of 2.0 A/g.

The electrochemical behaviors were evaluated by CV measurements (Figure S10). Compared with the PC materials, the oxidation peaks at 1.7 V and reduction peaks at 1.0 V ascribed to the doped S element in SPC materials is notable. Besides, all of samples exhibited reductive peaks at 0.5 V that can probably be attributed to the reduction of O element in 800-SPC materials [32,34,35]. The reductive peaks around 0.01 V were considered to be indicative of the impact of Na<sup>+</sup> on carbon layers [36,37]. Similar to general carbon materials, obvious charge-discharge plateaus were also not observed in any of the charge-discharge profiles of PC and SPC materials (Figure S8).

The linear fitting method was used to investigate the correlations among the structures and storage capacity (Figure S11). It is generally acknowledged that  $I_D/I_G$  values reflect the structural disorder and defect conditions. Therefore, a linear fitting of  $I_D/I_G$  values with storage capacity was conducted, and distinct linear relationships were clearly observed. This result also can indicate that the structural disorder and defects enhance the storage capacity. On the other hand, as shown in Figure S11b, the linear fitting relationships between the  $d_{002}$  and storage capacity indicated the expanded space can enhance the storage capacity. Therefore, the above analyses also explain the reasons that 800-SPC possessed more excellent storage capacity than other materials. In other words, these results verified that cooperative efforts of structural disorder, defects concentrations and  $d_{002}$  space play the main role to enhance the Na<sup>+</sup> storage capacity.

Furthermore, similar to a report by Zhou et al. [38], we adopt the ex situ method to evaluate the Na<sup>+</sup> storage contributions of different groups containing S element in the 800-SPC materials. After 800-SPC was subjected to a fully discharged status of 0.01 V, compared with the 800-SPC without discharge, the characteristic binding energies (163.8 and 165.0 eV) of  $-C-Sx-C$  groups shifted to 160.5 and 162.1 eV, respectively. Meanwhile, it is observed that the binding energies of  $-C-SOx-C$  were shifted from 167.5 to 167.0 eV. Considering the fact that SEI formed in the fully discharged case, we assume that the new fitting peak (159.3 eV) can probably be ascribed to the S contents in SEI (Figure S12).

On the other hand, after the 800-SPC was fully charged to 3.0 V, the binding energies of  $-C-Sx-C$  groups recovered to 163.3 and 164.8 eV, respectively. Meanwhile, the binding energies of  $-C-SOx-C$  recovered to 166.4 eV. According to the descriptions by Zhou et al. [38], analogous conversion tendencies on the binding energies of S-containing groups



were also observed in our studies (Table S8), indicating that partly irreversible reaction between Na and S also exist in 800-SPC materials. Because of the fact that the peak of the  $-C=S$  binding energy was covered by the SEI peak, the detailed storage contribution of  $-C=S$  groups cannot be clarified completely.

Together with the FT-IR results, we can infer that doping S element in coal tar pitch-based carbon causes an increase of the contents of  $-C-Sx-C$  and  $-C-SOx-C$  groups in the obtained carbon materials (Figure S2). The increased  $-C-Sx-C$  and  $-C-SOx-C$  groups assist in the  $Na^+$  storage processes and formation of SEI. However, a quantitative evaluation of the  $Na^+$  storage capacity of  $-C-Sx-C$  and  $-C-SOx-C$  groups cannot be carried out at the present stage. After searching for a more suitable evaluation method, we will investigate this topic in the future.

Finally, in accordance with the report by Wang et al., the storage mechanism was studied from the kinetics perspective [39–42]. As shown in Figure 7, compared with the 800-PC, the 800-SPC possessed a remarkable capacitive contribution, which was ascribed to the fact 800-SPC has a more suitable structure to enhance the capacitive contributions [43–45]. Combined with the above analyses, the increased capacitive contributions of 800-SPC can be facilely explained. Namely, as shown in Figure 8, the expanded distances of carbon layers provide fast channels to remove  $Na^+$ , and defects produced by S-doping provide the active sites which are beneficial to enhancing the capacitive effects [46,47].

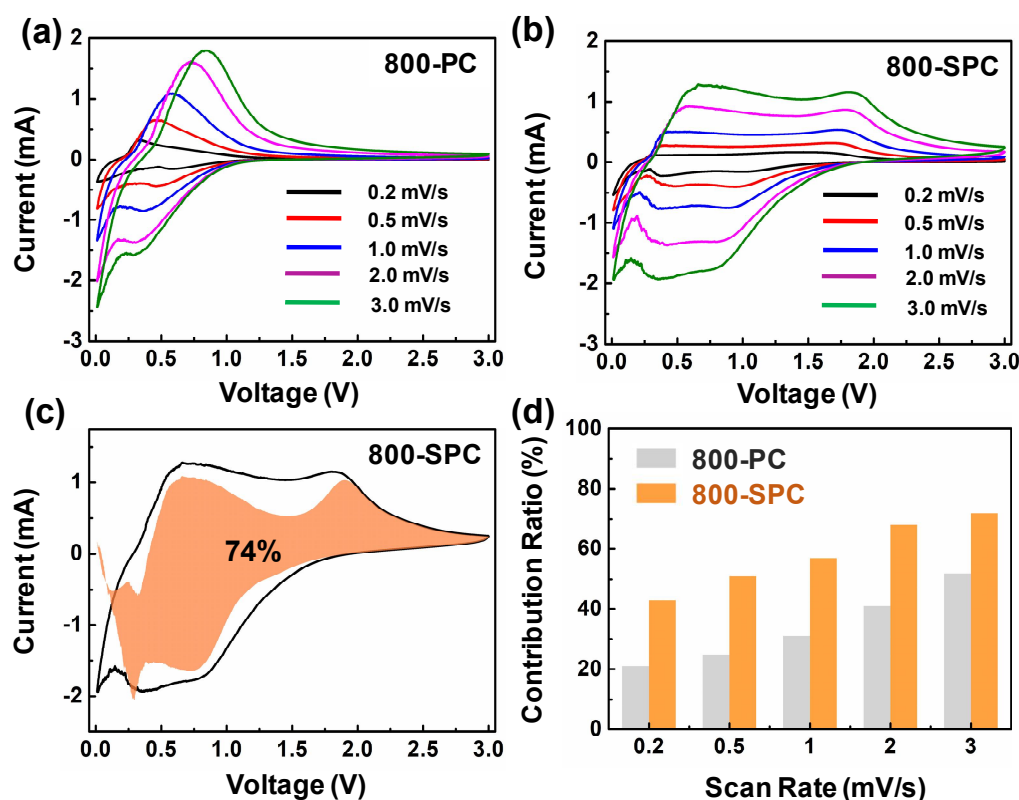


**Figure 7.** Capacitive contributions for storage capacity of 800-PC and 800-SPC materials. (a,b) respectively show the CV measurement results of 800-PC and 800-SPC materials at different scan rates. (c) shows the bar charts showing the capacitive contribution of 800-SPC at scan rate of 3.0 mV/s. (d) illustrates the capacitive contribution ratio of 800-PC and 800-SPC materials at different scan rates.

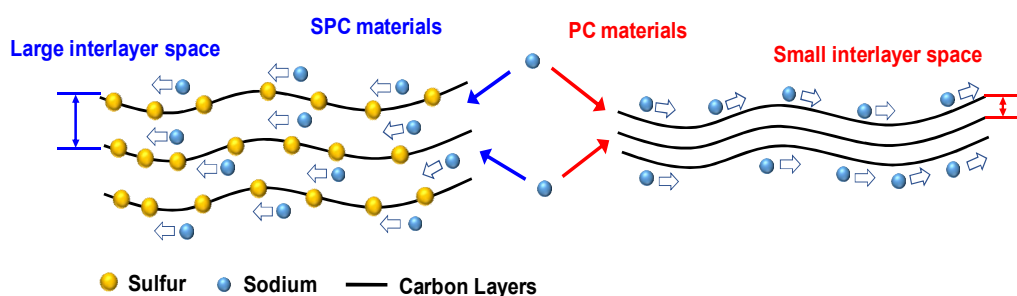


Figure 8. Images explaining the  $\text{Na}^+$  storage mechanism.

#### 4. Conclusions

The factors that influence the  $\text{Na}^+$  storage capacity of S-doped carbon materials were amply investigated through XPS, TEM and XRD measurements. Based on detailed investigations of the correlations between structures and  $\text{Na}^+$  storage capacity, it is observed that the structural disorder, carbon layer spacing and defect concentrations are the pivotal factors which influence the  $\text{Na}^+$  storage capacity of carbon materials. Therefore, controlling the carbonization temperature and using the S doping method made the 800-SPC material fabricated in our studies show an excellent storage capacity. The 800-SPC exhibits a storage capacity at 120 mAh/g after 2000 charge-discharge cycles were applied, when the current density was set at 2.0 A/g. We think that our studies can provide a useful reference for readers who are considering ideas to improve the  $\text{Na}^+$  storage capacity of soft carbon materials.

**Supplementary Materials:** The following are available online at <https://www.mdpi.com/article/10.3390/coatings11080948/s1>. Figure S1. XPS results of PC materials (a), Relationships between the O contents and carbonation temperatures (b). The contents of C-O, C=O and -COOH groups in PC materials (c–f), Figure S2. FT-IR results of PC and SPC materials, Figure S3. Investigations about the influence of temperature on the structures of PC (a) and SPC (b) materials by XRD measurements, Figure S4. TEM images and selected area electron diffraction (SAED) patterns of PC materials, Figure S5. TEM images and selected area electron diffraction (SAED) patterns of SPC materials, Figure S6. SEM morphologies of PC (a–d) and SPC (e–h) materials, and EDS mapping of (i) C, and (j) S, Figure S7. Pore size distribution curves of PC (a) and SPC (b) materials, Figure S8. Raman results of PC and SPC materials, Figure S9. Cycling performances of PC materials (a), Rate performances of PC materials (b), Cycling performances of SPC materials (c) and rate performances of SPC materials (d), Figure S10. CV profiles of PC materials (a–d) and SPC materials of (e–h) at scan rate of 0.5 mV/s. The charge-discharge measurement results of PC materials (a–d) and SPC materials of (e–h) are inserted into CV profiles, Figure S11. Illustrations of relationships of  $I_D/I_G$  and  $d_{002,a}$  with reversible capacity, Figure S12. XPS results of 800-SPC (a), fully discharged 800-SPC (b) and fully charged 800-SPC (c), Table S1. Fitted O 1s XPS results for PC samples, Table S2. Fitted S2p XPS results for SPC samples, Table S3. Element analysis results of PC and SPC materials, Table S4. The calculation results of R values, Table S5. Characteristic parameters about structures and specific surface areas of materials.  $S_{\text{BET}}$  = total BET surface area;  $V_{\text{total}}$  = total pore volume, Table S6. Fitted data from Raman results, Table S7. Comparisons of lithium storage properties of 800-SPC and other carbon materials in previous work, Table S8. Conversions of binding energies of 800-SPC, fully discharged 800-SPC and fully charged 800-SPC.

**Author Contributions:** Conceptualization, K.W. and W.Z.; methodology, K.W. and G.X.; validation, G.X. and B.H.; formal analysis, R.Y. and L.L.; investigation, R.Y. and B.H.; resources, S.L.; data curation, K.W.; writing—original draft preparation, R.Y.; writing—review and editing, W.Z.; supervision, D.J. and M.C.; project administration, B.A. All authors have read and agreed to the published version of the manuscript.

**Funding:** Not applicable.

**Institutional Review Board Statement:** Not applicable.

**Informed Consent Statement:** Not applicable.

**Data Availability Statement:** All the data is contained within the article or the Supplementary Material.

**Acknowledgments:** We are grateful to the supports of University of Science and Technology Liaoning (601009816-39) and 2017RC03. This work obtains the support by the Liaoning Province Education Department of China (Grant No.601009887-16). This work is partly supported with the project supported by the National Natural Science Foundation of China (Grant No. 51672117 and 51672118). This study is supported by Postdoctoral Foundation Project of Shenzhen Polytechnic 6020330007K.

**Conflicts of Interest:** The authors declare no conflict of interest.

## References

1. Min, X.; Xiao, J.; Fang, M.H.; Wang, W.; Zhao, Y.J.; Liu, Y.A.; Abdelkader, A.M.; Xi, K.; Kumar, R.V.; Huang, Z.H. Potassium-ion batteries: Outlook on present and future technologies. *Energy Environ. Sci.* **2021**, *14*, 2186–2243. [\[CrossRef\]](#)
2. Lu, S.Y.; Zhu, T.X.; Wu, H.; Wang, Y.K.; Li, J.; Abdelkader, A.; Xi, K.; Wang, W.; Li, Y.G.; Ding, S.J.; et al. Construction of ultrafine ZnSe nanoparticles on/in amorphous carbon hollow nanospheres with high-power-density sodium storage. *Nano Energy* **2019**, *59*, 762–772. [\[CrossRef\]](#)
3. Lu, S.Y.; Wu, H.; Hou, J.W.; Liu, L.M.; Li, J.; Harris, C.J.; Lao, C.Y.; Guo, Y.Z.; Xi, K.; Ding, S.J.; et al. Phase boundary engineering of metal-organic-framework-derived carbonaceous nickel selenides for sodium-ion batteries. *Nano Res.* **2020**, *13*, 2289–2298. [\[CrossRef\]](#)
4. Wang, S.; Zhang, X.B. N-Doped C@Zn<sub>3</sub>B<sub>2</sub>O<sub>6</sub> as a low cost and environmentally friendly anode material for Na-ion batteries: High performance and new reaction mechanism. *Adv. Mater.* **2018**, 1805432.
5. Zou, W.; Fan, C.; Li, J.Z. Sodium titanate/carbon (Na<sub>2</sub>Ti<sub>3</sub>O<sub>7</sub>/C) nanofibers via electrospinning technique as the anode of sodium-ion batteries. *Chin. J. Chem.* **2017**, *35*, 79–85. [\[CrossRef\]](#)
6. Kim, H.; Kim, H.; Zhang, D.; Myeong, H.L.; Kyungmi, L.; Gabin, Y.; Kisuk, K. Recent progress in electrode materials for sodium-ion batteries. *Adv. Energy Mater.* **2016**, *6*, 1600943. [\[CrossRef\]](#)
7. Zhang, S.; Zhang, J.; Wu, S.; Lv, W.; Kang, F.; Yang, Q. Research advances of carbon-based anode materials for sodium-ion batteries. *Acta Chim. Sin.* **2017**, *75*, 163–172. [\[CrossRef\]](#)
8. Qi, X.; Shah, H.; Nawaz, A.; Xie, W.; Muhammad, Z.A.; Batool, A.; Tian, L.; Saad, U.J.; Boddula, R.; Guo, B.; et al. Antibacterial carbon-based nanomaterials. *Adv. Mater.* **2019**, *8*, 1804838.
9. Bai, P.X.; He, Y.W.; Zou, X.X.; Zhao, X.X.; Xiong, P.X.; Xu, Y.H. Elucidation of the sodium-storage mechanism in hard carbons. *Adv. Energy Mater.* **2018**, *8*, 1703217. [\[CrossRef\]](#)
10. Chen, D.Q.; Zhang, W.; Luo, K.Y.; Song, Y.; Zhong, Y.J.; Liu, Y.X.; Wang, G.K.; Zhong, B.H.; Wu, Z.G.; Guo, X.D. Hard carbon for sodium storage: Mechanism and optimization strategies toward commercialization. *Energy Environ. Sci.* **2021**, *14*, 2244–2262. [\[CrossRef\]](#)
11. Qi, Y.R.; Lu, Y.X.; Ding, F.X.; Zhang, Q.Q.; Li, H.; Huang, X.J.; Chen, L.Q.; Hu, Y.S. Slope-dominated carbon anode with high specific capacity and superior rate capability for high safety Na-ion batteries. *Angew. Chem. Int. Ed.* **2019**, *58*, 4361–4365. [\[CrossRef\]](#) [\[PubMed\]](#)
12. Wang, Q.D.; Zhao, C.L.; Lu, Y.X.; Li, Y.M.; Zheng, Y.H.; Qi, Y.R.; Rong, X.H.; Jiang, L.W.; Qi, X.G.; Shao, Y.J.; et al. Advanced nanostructured anode materials for sodium-ion batteries. *Small* **2017**, *13*, 1701835. [\[CrossRef\]](#)
13. Moriwake, H.; Kuwabara, A.; Fiske, C.A.J.; Ikuhara, Y. Why is sodium-intercalated graphite unstable? *RSC Adv.* **2017**, *7*, 36550–36554. [\[CrossRef\]](#)
14. Cao, B.; Liu, H.; Xu, B.; Lei, Y.F.; Chen, X.H.; Song, H.H. Mesoporous soft carbon as an anode material for sodium ion batteries with superior rate and cycling performance. *J. Mater. Chem. A* **2016**, *4*, 6472–6478. [\[CrossRef\]](#)
15. Hao, M.; Xiao, N.; Wang, Y.; Li, H.; Zhou, Y.; Liu, C.; Qiu, J. Pitch-derived N-doped porous carbon nanosheets with expanded interlayer distance as high-performance sodium-ion battery anodes. *Fuel Process. Technol.* **2018**, *177*, 328–335. [\[CrossRef\]](#)
16. He, L.; Sun, Y.R.; Wand, C.L.; Guo, H.Y.; Guo, Y.Q.; Li, C.; Zhou, Y. High performance sulphur-doped pitch-based carbon materials as anode materials for sodium-ion batteries. *New Carbon Mater.* **2020**, *35*, 420–427. [\[CrossRef\]](#)
17. Li, W.; Zhou, M.; Li, H.; Wang, K.; Cheng, S.; Jiang, K. A high performance sulfur-doped disordered carbon anode for sodium ion batteries. *Energy Environ. Sci.* **2015**, *8*, 2916–2921. [\[CrossRef\]](#)
18. Xiao, L.; Cao, Y.; Henderson, W.A.; Sushko, M.L.; Shao, Y.; Xiao, J.; Wang, W.; Engelhard, M.H.; Nie, Z.; Liu, J. Hard carbon nanoparticles as high-capacity, high-stability anodic materials for Na-ion batteries. *Nano Energy* **2016**, *19*, 279–288. [\[CrossRef\]](#)
19. Yu, C.; Hou, H.; Liu, X.; Yao, Y.; Liao, Q.; Dai, Z.; Li, D. Old-loofah-derived hard carbon for long cyclic life anode in sodium ion battery. *Int. J. Hydrog. Energy* **2018**, *43*, 3253–3260. [\[CrossRef\]](#)
20. Saravanan, K.; Kalaiselvi, N. Nitrogen containing bio carbon as potential anode for lithium batteries. *Carbon* **2015**, *81*, 43–53. [\[CrossRef\]](#)
21. Qian, J.; Wu, F.; Ye, Y.; Zhang, M.; Huang, Y.X.; Xing, Y.; Qu, W.; Li, L.; Chen, R.J. Boosting fast sodium storage of a large-scalable carbon anode with an ultralong cycle life. *Adv. Energy Mater.* **2018**, *8*, 1703159. [\[CrossRef\]](#)

22. Liu, Y.; Xue, J.S.; Zheng, T.; Dahn, J.R. Mechanism of lithium insertion in hard carbons prepared by pyrolysis of epoxy resins. *Carbon* **1996**, *34*, 193–200. [\[CrossRef\]](#)
23. Luo, W.; Jian, Z.; Xing, Z.; Wang, W.; Bommier, C.; Lerner, M.M.; Ji, X. Electrochemically expandable soft carbon as anodes for Na-ion batteries. *ACS Cent. Sci.* **2015**, *1*, 516–522. [\[CrossRef\]](#)
24. Sun, N.; Guan, Z.; Liu, Y.W.; Cao, Y.L.; Zhu, Q.Z.; Liu, H.; Wang, Z.X.; Zhang, P.; Xu, B. Extended “adsorption–insertion” model: A new insight into the sodium storage mechanism of hard carbons. *Adv. Energy Mater.* **2019**, *9*, 1901351. [\[CrossRef\]](#)
25. Wu, S.Y.; Gu, J.; Zhang, X.; Wu, Y.Q.; Gao, J.S. Variation of carbon crystalline structures and CO<sub>2</sub> gasification reactivity of Shenfu coal chars at elevated temperatures. *Energy Fuels* **2008**, *22*, 199–206. [\[CrossRef\]](#)
26. Qiu, S.; Xiao, L.; Sushko, M.L.; Han, K.S.; Shao, Y.; Yan, M.; Liang, X.; Mai, L.; Feng, J.; Cao, Y.; et al. Manipulating adsorption–insertion mechanisms in nanostructured carbon materials for high-efficiency sodium ion storage. *Adv. Energy Mater.* **2017**, *7*, 1700403. [\[CrossRef\]](#)
27. Li, Z.W.; Zhong, J.L.; Chen, N.N.; Xue, B.; Mi, H.Y. Template-assisted preparation and lithium storage performance of nitrogen doped porous carbon sheets. *Acta Chim. Sin.* **2018**, *76*, 209–214. [\[CrossRef\]](#)
28. Xie, F.; Xu, Z.; Jensen, A.C.S.; Au, H.; Lu, Y.; Araullo-Peters, V.; Drew, A.J.; Hu, Y.S.; Titirici, M.M. Hard-Soft carbon composite anodes with synergistic sodium storage performance. *Adv. Funct. Mater.* **2019**, *29*, 1901072. [\[CrossRef\]](#)
29. Tong, Z.K.; Fang, S.; Zheng, H.; Zhang, X.G. Zn<sub>2</sub>GeO<sub>4</sub> nanorods@ graphene composite as anode materials for Li-ion batteries. *Acta Chim. Sin.* **2016**, *74*, 185–190. [\[CrossRef\]](#)
30. Ding, J.; Wang, H.; Li, Z.; Kohandehghan, A.; Cui, K.; Xu, Z.; Zahiri, B.; Tan, X.; Lotfabad, E.M.; Olsen, B.C.; et al. Carbon nanosheet frameworks derived from peat moss as high performance sodium ion battery anodes. *ACS Nano* **2013**, *7*, 11004–11015. [\[CrossRef\]](#)
31. Yao, X.; Ke, Y.; Ren, W.; Wang, X.; Xiong, F.; Yang, W.; Qin, M.; Li, Q.; Mai, L. Defect-Rich soft carbon porous nanosheets for fast and high-capacity sodium-ion storage. *Adv. Energy Mater.* **2018**, *9*, 1803260. [\[CrossRef\]](#)
32. Wang, N.N.; Wang, Y.X.; Xu, X.; Liao, T.; Du, Y.; Bai, Z.C.; Dou, S.X. Defect sites-rich porous carbon with pseudocapacitive behaviors as an ultrafast and long-term cycling anode for sodium-ion batteries. *ACS Appl. Mater. Interfaces* **2018**, *10*, 9353–9361. [\[CrossRef\]](#)
33. Yu, L.; Wang, L.P.; Liao, H.; Wang, J.; Feng, Z.; Lev, O.; Loo, J.S.C.; Sougrati, M.T.; Xu, Z.J. Understanding fundamentals and reaction mechanisms of electrode materials for Na-ion batteries. *Small* **2018**, *14*, 1703338. [\[CrossRef\]](#)
34. Chen, L.; Bai, L.; Yeo, J.; Wei, T.; Chen, W.; Fan, Z. Wood-derived carbon with selectively introduced C=O groups toward stable and high capacity anodes for sodium storage. *ACS Appl. Mater. Interfaces* **2020**, *12*, 27499–27507. [\[CrossRef\]](#) [\[PubMed\]](#)
35. Chen, W.M.; Chen, C.J.; Xiong, X.Q.; Hu, P.; Hao, Z.X.; Huang, Y.H. Coordination of surface-induced reaction and intercalation: Toward a high-performance carbon anode for sodium-ion batteries. *Adv. Sci.* **2017**, *4*, 1600500. [\[CrossRef\]](#) [\[PubMed\]](#)
36. Yang, B.; Chen, J.; Lei, S.; Guo, R.; Li, H.; Shi, S.; Yan, X. Spontaneous growth of 3d framework carbon from sodium citrate for high energy- and power-density and long-life sodium-ion hybrid capacitors. *Adv. Energy Mater.* **2018**, *8*, 1702409. [\[CrossRef\]](#)
37. Zhang, Y.; Li, X.; Dong, P.; Wu, G.; Xiao, J.; Zeng, X.; Zhang, Y.; Sun, X. Honeycomb-like hard carbon derived from pine pollen as high-performance anode material for sodium-ion batteries. *ACS Appl. Mater. Interfaces* **2018**, *10*, 42796–42803. [\[CrossRef\]](#) [\[PubMed\]](#)
38. Wang, Q.Q.; Ge, X.F.; Xu, J.Y.; Du, Y.C.; Zhao, X.; Si, L.; Zhou, L.S. Fabrication of microporous sulfur-doped carbon microtubes for high-performance sodium-ion batteries. *ACS Appl. Energy Mater.* **2018**, *1*, 6638–6645. [\[CrossRef\]](#)
39. Choi, C.; Ashby, D.S.; Butts, D.M.; DeBlock, R.H.; Wei, Q.; Lau, J.; Dunn, B. Achieving high energy density and high power density with pseudocapacitive materials. *Nat. Rev. Mater.* **2019**, *5*, 5–19. [\[CrossRef\]](#)
40. Wang, K.; Ju, D.Y.; Xu, G.Y.; Han, B.B.; Chai, M.R.; Wang, Y.X.; Li, L.X.; Zhang, X.H.; Ucida, M.; Zhou, W.M. Organosilicon modified method to improve Li<sup>+</sup> storage capacity of graphene oxide (GO). *Sci. China Technol. Sci.* **2020**, *63*, 2709–2716. [\[CrossRef\]](#)
41. Wang, J.; Polleux, J.; Lim, J.; Dunn, B. Pseudocapacitive contributions to electrochemical energy storage in TiO<sub>2</sub> (anatase) nanoparticles. *J. Phys. Chem. C* **2007**, *111*, 14925–14931. [\[CrossRef\]](#)
42. Augustyn, V.; Come, J.; Lowe, M.A.; Kim, J.W.; Taberna, P.L.; Tolbert, S.H.; Abruna, H.D.; Simon, P.; Dunn, B. High-rate electrochemical energy storage through Li<sup>+</sup> intercalation pseudocapacitance. *Nat. Mater.* **2013**, *12*, 518–522. [\[CrossRef\]](#) [\[PubMed\]](#)
43. Chao, D.L.; Zhu, C.R.; Yang, P.H.; Xia, X.H.; Liu, J.L.; Wang, J.; Fan, X.F.; Savilov, S.V.; Lin, J.; Fan, H.J.; et al. Array of nanosheets render ultrafast and high-capacity Na-ion storage by tunable pseudocapacitance. *Nat. Commun.* **2016**, *7*, 12122. [\[CrossRef\]](#) [\[PubMed\]](#)
44. Kim, H.S.; Cook, J.B.; Tolbert, S.H.; Dunn, B. The development of pseudocapacitive properties in nanosized-MoO<sub>2</sub>. *J. Electrochem. Soc.* **2015**, *162*, 5083–5090. [\[CrossRef\]](#)
45. Simon, P.; Gogotsi, Y.; Dunn, B. Where do batteries end and supercapacitors begin? *Science* **2014**, *343*, 1210–1211. [\[CrossRef\]](#)
46. Cui, C.; Wang, H.; Wang, M.; Ou, X.; Wei, Z.; Ma, J.; Tang, Y. Hollow carbon nanobelts codoped with nitrogen and sulfur via a self-templated method for a high-performance sodium-ion capacitor. *Small* **2019**, *15*, 1902659. [\[CrossRef\]](#)
47. Jeon, I.Y.; Zhang, S.; Zhang, L.; Choi, H.J.; Seo, J.M.; Xia, Z.; Dai, L.; Baek, J.B. Edge-selectively sulfurized graphenenanoplatelets as efficient metal-free electrocatalysts for oxygen reduction reaction: The electron spin effect. *Adv. Mater.* **2013**, *25*, 6138–6145. [\[CrossRef\]](#)